Impact of iterative reconstructions on image quality and detectability of focal liver lesions in low-energy monochromatic images

J. Greffier, J. Frandon, A. Hamard, J.M. Teissier, H. Pasquier, J.P. Beregi, D. Dabli

To cite this version:

J. Greffier, J. Frandon, A. Hamard, J.M. Teissier, H. Pasquier, et al.. Impact of iterative reconstructions on image quality and detectability of focal liver lesions in low-energy monochromatic images. Physica Medica, 2020, 77, pp.36-42. 10.1016/j.ejmp.2020.07.024 . hal-03340961

HAL Id: hal-03340961

https://hal.umontpellier.fr/hal-03340961

Submitted on 22 Aug 2022

HAL is a multi-disciplinary open access archive for the deposit and dissemination of scientific research documents, whether they are published or not. The documents may come from teaching and research institutions in France or abroad, or from public or private research centers.

L'archive ouverte pluridisciplinaire **HAL**, est destinée au dépôt et à la diffusion de documents scientifiques de niveau recherche, publiés ou non, émanant des établissements d'enseignement et de recherche français ou étrangers, des laboratoires publics ou privés.

Distributed under a Creative Commons Attribution 4.0 International License

Version of Record: https://www.sciencedirect.com/science/article/pii/S1120179720301848
Manuscript_3daf4cee1c57e7cd92baf1a38d07879a

Impact of iterative reconstructions on image quality and detectability of focal liver lesions in low-energy monochromatic images.

J. Greffier[1,*], J. Frandon[1], A. Hamard[1], J.M. Teissier[2], H. Pasquier[3], J.P. Beregi[1,2], D. Dabli[1].

1. Department of medical imaging, CHU Nimes, Univ Montpellier, Medical Imaging Group Nimes, EA 2415, Nîmes, France

2. Service d'imagerie médicale, GIE Imagerie, Institut de Cancérologie du Gard, Nîmes, France

3. GE Healthcare, Buc, France

* Corresponding author:

Joël Greffier, CHU de Nîmes, Medical Imaging Group Nîmes, EA 2415, Bd Prof Robert Debré, 30029 Nîmes Cedex 9; tel: +33.466.683.309; fax: +33.466.683.308; email: joel.greffier@chu-nimes.fr

© 2020 published by Elsevier. This manuscript is made available under the CC BY NC user license
https://creativecommons.org/licenses/by-nc/4.0/

Impact of iterative reconstructions on image quality and detectability of focal liver lesions in low-energy monochromatic images.

Abstract

Purpose

To assess the impact of iterative reconstructions on image quality and detectability of focal liver lesions in low-energy monochromatic images from a Fast kV-Switching Dual Energy CT platform (KVSCT).

Methods

Acquisitions on an image-quality phantom were performed using a KVSCT for three dose levels ($CTDI_{vol}$:12.72/10.76/8.79mGy). Raw data were reconstructed for five energy levels (40/50/60/70/80keV) using Filtered Back Projection (FBP) and four levels of ASIR (ASIR30/ASIR50/ASIR70/ASIR100). Noise power spectrum (NPS) and task-based transfer function (TTF) were measured before computing a Detectability index (*d'*) to model the detection task of liver metastasis (LM) and hepatocellular carcinoma (HCC) as function of keV.

Results

From 40 to 70keV, noise-magnitude was reduced on average by -68%±1% with FBP; -61%±3% with ASIR50 and -52%±6% with ASIR100. The mean spatial frequency of the NPS decreased when the energy level decreased and the iterative level increased. TTF values at 50% decreased as the energy level increased and as the percentage of ASIR increased. The detectability of both lesions increased with increasing dose level and percentage of ASIR. For the LM, *d'* peaked at 70keV for all reconstruction types, except for ASIR70 at 12.72mGy and ASIR100, where *d'* peaked at 50 keV. For HCC, *d'* peaked at 60keV for FBP and ASIR30 but peaked at 50 keV for ASIR50, ASIR70 and ASIR100.

Conclusions

Using percentage of ASIR above 50% at low-energy monochromatic images could limit the increase of noise-magnitude, benefit from spatial resolution improvement and hence enhance detectability of subtle low contrast focal liver lesions such as HCC.

Keywords

Multidetector Computed tomography; Dual-energy; Iterative reconstruction; Task-based image quality assessment.

Abbreviations

ASIR: Adaptive Statistical Iterative Reconstruction

CT: Computed Tomography

CTDI_{vol}: Volume CT dose index

d’: Detectability index

DECT: Dual-energy CT

ESF: Edge spread function

FBP: Filtered Back Projection

HCC: Hepatocellular carcinoma

IR: Iterative reconstruction

KVSCT: Fast kV switching CT

LM: Liver metastasis

LSF: Line spread function

NPS: Noise power spectrum

SECT: Single-energy CT

TTF: Task-based transfer function

Introduction

Dual-Energy CT (DECT) is increasingly used in clinical practice [1-9]. It is based on the attenuation difference of various materials as a function of energy [5, 10]. The principle of DECT imaging is to use both low- and high-energy photon spectra to calculate the photoelectric and Compton scattering effects separately in order to obtain the attenuation difference of various materials as a function of energy [5, 10]. DECT is particularly useful in abdominal indications by generating virtual monochromatic images. Many studies have shown the advantage of using 50-60 keV energy levels for the detection and characterization of hepatic, pancreatic or renal lesions in abdominal imaging [1-4, 6, 11]. Compared to 70 keV simulating 120 kVp Single-Energy CT (SECT) [12], images obtained with lower monochromatic levels enhanced the iodine contrast in these lesions. Several DECT platforms exist with different acquisition techniques to obtain both low- and high-energy photon spectra. Among those, Gemstone Spectral Imaging (GSI – GE Healthcare) is a fast kVp switching CT (KVSCT) technique that uses one X-ray tube / detector pair and switches from 80 to 140 kVp in less than 0.5 milliseconds [3, 4, 13]. The tube current (mA) is fixed and the exposure time is adjusted to obtain an uniform distribution of the dose between both kVp.

Several studies on phantoms and patients have evaluated the spectral performance of GSI on Filtered Back Projection (FBP) images using classical metrics such as the accuracy of HU values and the iodine bias [12, 14-16]. However, Iterative Reconstruction (IR) algorithms such as Adaptive Statistical Iterative Reconstruction (ASIR) are now available and used routinely on DECT platforms, especially for low-energy monochromatic images to decrease the noise magnitude. ASIR reconstructs the CT projections by including the system statistics in the process and using an FBP image as a building block for each individual image reconstruction [17]. ASIR incorporates matrix algebra to convert the measured value of each pixel to an updated estimate of the pixel value. This pixel value is then evaluated and compared to the ideal value that is predicted with noise statistics. Those steps are repeated iteratively until the difference between the final estimation and the ideal pixel values is inferior to a stopping threshold. The ASIR image is then reconstructed and blended with traditional FBP in 10% increments according to user preference.

Many studies performed on SECT have shown that specifically-adapted metrics must be used when assessing the image quality of IR [18-21]. Hence, a task-based image quality assessment is now commonly applied in routine when considering IR. It employs metrics such as the Noise Power Spectrum (NPS) to assess both the magnitude and texture of the noise; and the Task-based Transfer function (TTF) to evaluate the spatial resolution. A detectability index (*d'*) can then be computed to estimate the radiologist's ability to perform a clinical task. The detectability index value reflects the noise and resolution properties (NPS and TTF outcomes) as they relate to the ability of the system to perform a task of interest.

The purpose of this study was to assess the impact of ASIR on GSI low-energy monochromatic images by measuring the noise characteristics, spatial resolution and detectability of small focal liver lesions.

Materials and methods

Phantoms used

A 20-cm-diameter ACR QA phantom (Gammex 464, Middleton, WI) placed inside a body ring (diameter of 33 cm and length of 24 cm) (**Figure 1.a**) was scanned to measure the NPS (**Figure 1.b**), the TTF (**Figure 1.c**) and detectability indexes.

Acquisition and reconstruction parameters

Acquisitions were performed on a fast KVSCT system (Revolution HD, GE Healthcare). Three GSI presets adapted to abdominal imaging were used, resulting in $\mathrm{CTDI}_{\mathrm{vol}}$ of 12.72, 10.76 and 8.79 mGy, respectively. These three dose levels correspond to the 75th, 50th and 25th percentiles of the data distribution used to define our national Diagnostic Reference Level for abdomen-pelvic CT examination, respectively. Detailed acquisition parameters of each GSI preset are listed in **Table 1**.

Raw data were reconstructed using FBP and ASIR at 30, 50, 70 and 100% levels for five monochromatic energy levels (40, 50, 60, 70 and 80 keV). Images were reconstructed with the standard reconstruction kernel, a slice thickness of 1.25 mm (1.25 mm increment) and a field of view of 250 mm.

Noise power spectrum

Noise characteristics were measured by NPS, using module 3 of the ACR phantom. For each reconstruction, four 128×128 pixels regions of interest (ROIs) within 20 consecutive axial slices of the module were used to compute the 2D-NPS. Each ROI was detrended by subtracting a fitted 2D second-order paraboloid to remove the low-frequency non-uniformity caused by x-ray scatter and beam hardening [22]. The 2D-NPS was then computed as the area-normalized Fourier transform of the ROI [23]:

$$\mathrm{NPS}(f_x, f_y) = \frac{\Delta_x \Delta_y}{N_x N_y} \frac{\sum_{i=1}^{N_{ROI}} |F[\mathrm{ROI}_i(x,y) - \mathrm{FIT}_i(x,y)]|^2}{N_{ROI}}, \qquad (1)$$

where Δ_k and N_k denote respectively the pixel size and the number of pixels of a ROI along axis k respectively; $F[\ldots]$ corresponds to the 2D Fourier transform; $ROI_i(x, y)$ is the ith ROI in the spatial domain; $FIT_i(x, y)$ is the 2D second-order paraboloid fit of the ith ROI and N_{ROI} is the total number of ROIs. 2D-NPS measurements were radially averaged and binned into 64 frequency bins to provide 1D-NPS curves. To quantify the changes of magnitude and texture of noise between reconstructions, the square root of the Area Under the Curve and average spatial frequency of the NPS curve (f_{av}) were measured respectively.

Task-based transfer function

Spatial resolution was assessed using a TTF in module 1 of the ACR phantom from 15 consecutive axial slices according to the methodology previously reported [24] and [18, 20].

TTF was computed only on the acrylic insert to be close to the contrast of the two simulated lesions for the detectability index computation. A ROI was placed around this, and a circular-edge technique was employed to measure the edge spread function (ESF) by plotting the N_{CT} of each pixel as a function of the distance to the center of the insert. The line spread function (LSF) was then obtained by derivation of the ESF. The TTF was computed from the normalized Fourier transformation of the LSF. To quantify the loss/benefit of spatial resolution between reconstructions, the spatial frequency at which the TTF reduced to 50% (f_{50}) was measured [25].

Detectability

A detectability index (d') was computed to assess the detection of liver metastasis and hepatocellular carcinoma as function of energy level, iterative level and dose level. Detectability combines resolution and noise characteristics of an imaging system with a predefined function, noted W_{task}, representative of a clinical imaging task to estimate how well a human observer would perform the considered task [20].

This index was based on a Non PreWhitening matched filter with Eye filter and Internal noise (NPWEi) model observer as [24, 26]:

$$d'^2_{NPWEi} = \frac{\left[\iint MTF^2_{task}(u,v)W^2_{task}(u,v)E^2(u,v)dudv\right]^2}{\iint NPS(u,v)MTF^2_{task}(u,v)W^2_{task}(u,v)E^4(u,v) + MTF^2_{task}(u,v)W^2_{task}(u,v)N_i(u,v)dudv}, \quad (2)$$

where u and v are the spatial frequencies, $E(u,v)$ is the eye filter and N_i denotes the internal noise. The eye filter employed in this study was identical to the one used by Burgess *et al.*[25], which was modeled on the contrast sensitivity function curve measured by Barten *et al.* for the human visual system [27]:

$$E(f) = f^n \exp(-cf^2), \quad (3)$$

where f designates the radial spatial frequency such as $f^2 = u^2 + v^2$. Setting n as 1.3 has been shown to yield good agreement with measurements and the value of c is determined such that $E(f)$ peaks at four cycles/degree for a viewing distance set to 40 cm [28, 29]; here $c \approx 3$. Assuming that the NPS is constant, the internal noise was considered uncorrelated and defined as a fraction (0.02 at a viewing distance of 100 cm) [25] of the NPS scaled to the observer's viewing distance D:

$$N_i(u,v) = 0.02\left(\frac{D}{100}\right)^2 NPS. \quad (4)$$

W_{task} is a mathematical function representative of a given imaging task in the frequency domain. It is given by the Fourier transform of the difference between the signal present $h_1(x,y)$ and signal absent $h_2(x,y)$ hypotheses [20, 23]:

$$W_{task}(u,v) = F[h_1(x,y) - h_2(x,y)]\,. \quad (5)$$

Two task functions were defined to model the detection task of a liver metastasis (LM) and hepatocellular carcinoma (HCC). These task functions were assumed to represent a circular signal with a diameter of 10 mm. To account for lesion enhancement variation as a function of keV, the contrast between each clinical task and the liver parenchyma was defined according to the curves of HU variations measured on patients and published by Wang *et al.* for LM, HCC and the liver parenchyma [6] (**Table 2**).

For each detection task, d' values obtained at 40, 50 and 60 keV were compared with those obtained for a SECT acquisition at 120 kVp with the same acquisition and reconstruction parameters.

Results

Noise power spectrum

Noise magnitude

Overall, for all three GSI presets, noise magnitude decreased as the dose increased (**Figure 2**). Across the monochromatic energy range considered, for the three GSI presets and all reconstructions, the noise magnitude decreased from 40 keV to a minimum at 70 keV and then increased at 80 keV. From 40 to 70 keV, noise magnitude was reduced on average by -68%±1% with FBP; -61%±3% with ASIR50 and -52%±6% with ASIR100.

At all energy levels, the noise magnitude was inferior with iterative reconstruction and further decreased when increasing the percentage of ASIR. The difference in noise reduction using ASIR compared to FBP was greatest at 40 keV and decreased as the monochromatic energy increased. The noise reductions with the different ASIR levels compared to FBP were similar at all dose levels. On average, noise magnitude was reduced by -39%±2% with ASIR50 and -66%±2% with ASIR100 at 40 keV and -26%±1% and -49%±2% at 70 keV, respectively.

Noise texture

The noise texture was impacted by the monochromatic energy level of the reconstructed images. Across the energy range considered, for all doses and reconstruction algorithms, the f_{av} of the NPS was the greatest and therefore most favorable at 70 keV (**Figure 3**). The f_{av} of the NPS shifted towards higher frequencies from 40 to 70 keV and shifted towards lower frequencies from 70 to 80 keV.

Comparing the different reconstructions, the f_{av} of the NPS shifted towards lower frequencies when the percentage of ASIR increased. The impact of the proportion of ASIR on noise texture was increased at lower energy but equivalent at all dose levels. Compared to FBP, f_{av} of the NPS was reduced on average by 28%±2% with ASIR50 and 54%±2% with ASIR100 at 40 keV and 13%±0% and 28%±1% at 70 keV, respectively.

Task-based transfer function

The values of TTF at 50% (f_{50}) decreased as the energy level increased and as the percentage of ASIR increased (**Figure 4**). From 40 to 80 keV, f_{50} decreased on average from 0.61 mm^{-1} to 0.24 mm^{-1} for FBP, from 0.57 mm^{-1} to 0.22 mm^{-1} for ASIR50 and from 0.39 mm^{-1} to 0.22 mm^{-1} for ASIR100. Spatial resolution wasn't impacted by the dose.

Detectability index

Figure 5 depicts the detectability index (*d'*) obtained for the two simulated lesions as function of the energy level for each dose level and percentage of ASIR. Overall, the detectability of the two considered lesions increased with increasing dose level and percentage of ASIR.

For the LM, *d'* increased from 40 keV to 70 keV and decreased afterwards for FBP, ASIR30 and ASIR50. Using ASIR70 for GSI 40 and GSI 22, the detectability also peaked at 70 keV. However, for GSI 1, *d'* tended to increase with decreasing energy, peaking at 50 keV. Similarly, for ASIR100, highest *d'* values were found at 50 keV and detectability between 50 and 70 keV increased with the dose level (3% for GSI 40 and 23% for GSI 1).

For the HCC, when using FBP or ASIR30, *d'* peaked at 60 keV. For higher iterative percentage, from ASIR50 to ASIR100, *d'* increased when decreasing the monochromatic energy, peaking at 50 keV. The improvement of *d'* between 50 and 70 keV decreased when the dose level and the percentage of ASIR decreased (for GSI 40: 33% with ASIR100 and 5% with ASIR50; for GSI 1: 67% with ASIR100 and 22% with ASIR50).

d' value variations for both detection tasks from 40 to 60 keV were compared to that a SECT acquisition at 120 kVp (**Table 3**). For the LM, the *d'* values were higher than those obtained at 120 kVp at all dose levels when using ASIR70 and ASIR100 at 60 and 50 keV For GSI 1, resulting in the highest dose level, the detectability of the LM was also increased for ASIR30 and ASIR50 at 60 keV and for ASIR50 at 50 keV.. For the HCC, the *d'* values obtained at 60 keV were higher than for a SECT acquisition at 120 kVp for reconstruction types and dose levels. At 50 keV, the *d'* values were higher only for ASIR50 for GSI 22 and GSI 1, for ASIR70 and ASIR100 at all dose levels.

Discussion

This study confirmed on GSI DECT images the same behavior of ASIR previously found on SECT images [18, 20]. For a given energy level, the use of ASIR reduced the noise magnitude but decreased the spatial resolution and changed the image texture by increasing its smoothness. In addition, ASIR improved the detectability of the two simulated lesions and favored the use of low keV monochromatic images compared to the conventional SECT polychromatic 120 kVp images.

In the present study, a task-based image quality assessment was used to evaluate the image quality of spectral images using IR algorithms. Indeed, the use of these IR algorithms requires to assess the image quality more completely than with conventional metrics such as noise, SNR or CNR. These metrics are used to simply evaluate the image quality but do not take into account changes in noise texture or the dependence of spatial resolution on dose and contrast on IR images. For this, new metrics such as the NPS, the TTF or the detectability index are used. Many studies have shown the interest and the superiority of these new metrics in the analysis of IR images and in the optimization process compared to classical metrics [18, 20, 21, 30-34].

Our NPS results showed that noise magnitude increased from 70 to 40 keV and the average frequency of the f_{av} of the NPS shifted towards lower frequencies. Similar results have been found by Zang *et al.* with the KVSCT technique but with a $CTDI_{vol}$ close to 26 mGy [7]. These results are linked to the decrease in the average beam energy when the keV decreases, which reduces the penetration power of the X-ray beam and therefore increases the image noise. For a given energy level, the variations in NPS outcomes as a function of the dose and the percentage of ASIR are similar to those published on SECTs [18-20]. Noise magnitude decreased as the dose and percentage of ASIR increased. Conversely, f_{av} of the NPS decreased (i.e. noise texture got smoother) with increasing percentage of ASIR, but was only weakly influenced by the dose.

Our TTF outcomes show that the highest values of f_{50} were found at 40 keV and then spatial resolution decreased to lower values as energy increased. This variation of the TTF as a function of the keV is due to the enhancement on the border of the acrylic insert, particularly at lowest energy levels. This enhancement introduces an overshoot on the ESF curves, which improves the TTF and therefore the spatial resolution. As for the NPS, for a given energy level, the TTF variations as a function of the dose and the percentage of ASIR are similar to those published on SECTs [18, 20, 32]. Values of f_{50} were not changed by the dose level, but decreased as the percentage of ASIR increased.

The outcomes of detectability index showed that *d'* values increased when the dose and the percentage of ASIR increased, regardless of the energy level used. Similar results were found with ASIR on SECTs for one energy level [18, 20]. The values of *d'* varied in different ways with keV as function of the percentage of ASIR and the simulated lesion. For the LM, the detectability was highest at 70 keV and did not increase with monochromatic images of lower energy reconstructed with FBP and ASIR up to 50%. Conversely, for ASIR100, the detectability decreased when lowering the energy and peaked at 50 keV. For HCC, the use of ASIR improved detectability when reducing the energy to 60 keV for FBP and ASIR30 and to 50 keV for higher ASIR percentages. These differences between lesions were directly related to the NPS and TTF outcomes and the contrast variations of the simulated lesions. With a lower contrast, the detectability of the HCC was lower than that of LM and more dependent on noise and spatial resolution variations. The reduction of the noise magnitude associated with mid-to-high percentages of ASIR benefited from the increase of lesion contrast and spatial resolution (TTF) at low keV to improve detection. However, because the contrast between the metastasis and the surrounding liver parenchyma is already sufficient at 120 kVp, the detectability of such lesions can be further improved at low-energy only when using the highest percentage of ASIR.

The results found in this study showed that it was possible and beneficial, to use ASIR to reduce image noise and promote the use of low keV for the detection of focal liver lesions in portal venous phase. Indeed, many clinical studies have shown the advantage of using energy levels between 50 and 60 keV for the detection and characterization of hepatic, pancreatic or renal lesions in abdominal imaging [1-4, 6, 11]. Using these energy levels, the photoelectric effect was then predominant, enhancing the lesion with iodine contrast. However, the results of this present study showed that image texture became smoother when lowering the energy of virtual monochromatic images.

This study has several limitations. Firstly, despite increasing the phantom attenuation to more closely resemble that of a patient, it was made of relatively uniform and geometric structures, which do not perfectly represent human anatomy. Furthermore, the use of this phantom does not take into account the movements of organs or tissues of the upper abdomen due to breathing during CT acquisitions. These movements could blur images and hence affect the detectability of small liver lesions. Further patients study should be conducted to confirm the results found on this phantom study Moreover, acquisitions were performed for a single standard reconstruction kernel, for specific GSI presets and on a single CT scan. Only two types of lesions were simulated with a fixed size. The evaluation of other acquisition/reconstruction parameters combinations and lesion characteristics representative of all vascular phases would be necessary to fully assess the performance of ASIR in low-energy monochromatic images. Finally, a new GSI platform (GSI Xtream) has been developed on more recent CT systems from the same CT vendor. It differs in the acquisition and detection process and enables the newest generation of iterative reconstruction (ASIR-V) which has demonstrated better performance in SECT [18, 35, 36]. A future study should be conducted to assess the changes in the metrics studied between the two platforms.

Conclusion

Our phantom-based study demonstrated that using percentage of ASIR above 50% at low-energy monochromatic images could limit the increase of the noise magnitude and benefit from spatial resolution improvement. Hence, it could enhance detectability of subtle low contrast focal liver lesions, such as HCC.

Acknowledgements

We thank S. KABANI for her help in editing the manuscript.

The authors state that this work has not received any funding. One author declares relationship with the following company: GE Healthcare. H. PASQUIER is a GE Healthcare employee. However, he neither had access nor control on the phantom data acquisition and analysis. All other authors of this manuscript declare no relationships with any companies, whose products or services may be

related to the subject matter of the article.

References

[1] De Cecco CN, Boll DT, Bolus DN, Foley WD, Kaza RK, Morgan DE, et al. White Paper of the Society of Computed Body Tomography and Magnetic Resonance on Dual-Energy CT, Part 4: Abdominal and Pelvic Applications. J Comput Assist Tomogr. 2017;41:8-14.

[2] Agrawal MD, Pinho DF, Kulkarni NM, Hahn PF, Guimaraes AR, Sahani DV. Oncologic applications of dual-energy CT in the abdomen. Radiographics. 2014;34:589-612.

[3] Goo HW, Goo JM. Dual-Energy CT: New Horizon in Medical Imaging. Korean J Radiol. 2017;18:555-69.

[4] Marin D, Boll DT, Mileto A, Nelson RC. State of the art: dual-energy CT of the abdomen. Radiology. 2014;271:327-42.

[5] McCollough CH, Leng S, Yu L, Fletcher JG. Dual- and Multi-Energy CT: Principles, Technical Approaches, and Clinical Applications. Radiology. 2015;276:637-53.

[6] Wang Q, Shi G, Qi X, Fan X, Wang L. Quantitative analysis of the dual-energy CT virtual spectral curve for focal liver lesions characterization. Eur J Radiol. 2014;83:1759-64.

[7] Zhang D, Li X, Liu B. Objective characterization of GE discovery CT750 HD scanner: gemstone spectral imaging mode. Med Phys. 2011;38:1178-88.

[8] Matsumoto K, Jinzaki M, Tanami Y, Ueno A, Yamada M, Kuribayashi S. Virtual monochromatic spectral imaging with fast kilovoltage switching: improved image quality as compared with that obtained with conventional 120-kVp CT. Radiology. 2011;259:257-62.

[9] Yu L, Christner JA, Leng S, Wang J, Fletcher JG, McCollough CH. Virtual monochromatic imaging in dual-source dual-energy CT: radiation dose and image quality. Med Phys. 2011;38:6371-9.

[10] Alvarez RE, Macovski A. Energy-selective reconstructions in X-ray computerized tomography. Phys Med Biol. 1976;21:733-44.

[11] Chandarana H, Megibow AJ, Cohen BA, Srinivasan R, Kim D, Leidecker C, et al. Iodine quantification with dual-energy CT: phantom study and preliminary experience with renal masses. AJR Am J Roentgenol. 2011;196:W693-700.

[12] Jacobsen MC, Schellingerhout D, Wood CA, Tamm EP, Godoy MC, Sun J, et al. Intermanufacturer Comparison of Dual-Energy CT Iodine Quantification and Monochromatic Attenuation: A Phantom Study. Radiology. 2018;287:224-34.

[13] Siegel MJ, Kaza RK, Bolus DN, Boll DT, Rofsky NM, De Cecco CN, et al. White Paper of the Society of Computed Body Tomography and Magnetic Resonance on Dual-Energy CT, Part 1: Technology and Terminology. J Comput Assist Tomogr. 2016;40:841-5.

[14] Jacobsen MC, Cressman ENK, Tamm EP, Baluya DL, Duan X, Cody DD, et al. Dual-Energy CT: Lower Limits of Iodine Detection and Quantification. Radiology. 2019;292:414-9.

[15] Sellerer T, Noel PB, Patino M, Parakh A, Ehn S, Zeiter S, et al. Dual-energy CT: a phantom comparison of different platforms for abdominal imaging. Eur Radiol. 2018;28:2745-55.

[16] Washio H, Ohira S, Karino T, Nitta Y, Hayashi M, Miyazaki M, et al. Accuracy of Quantification of Iodine and Hounsfield Unit Values on Virtual Monochromatic Imaging Using Dual-Energy Computed Tomography: Comparison of Dual-Layer Computed Tomography With Fast Kilovolt-Switching Computed Tomography. J Comput Assist Tomogr. 2018;42:965-71.

[17] Geyer LL, Schoepf UJ, Meinel FG, Nance JW, Jr., Bastarrika G, Leipsic JA, et al. State of the Art: Iterative CT Reconstruction Techniques. Radiology. 2015;276:339-57.

[18] Greffier J, Frandon J, Larbi A, Beregi JP, Pereira F. CT iterative reconstruction algorithms: a task-based image quality assessment. Eur Radiol. 2020;30:487-500.

[19] Greffier J, Larbi A, Frandon J, Moliner G, Beregi JP, Pereira F. Comparison of noise-magnitude and noise-texture across two generations of iterative reconstruction algorithms from three manufacturers. Diagn Interv Imaging. 2019;100:401-10.

[20] Samei E, Richard S. Assessment of the dose reduction potential of a model-based iterative reconstruction algorithm using a task-based performance metrology. Med Phys. 2015;42:314-23.

[21] Verdun FR, Racine D, Ott JG, Tapiovaara MJ, Toroi P, Bochud FO, et al. Image quality in CT: From physical measurements to model observers. Phys Med. 2015;31:823-43.

[22] Zhou Z, Gao F, Zhao H, Zhang L. Techniques to improve the accuracy of noise power spectrum measurements in digital x-ray imaging based on background trends removal. Med Phys. 2011;38:1600-10.

[23] Measurements. ICoRUa. Medical imaging - the assessment of image quality. . ICRU Report No 54 Bethesda, MD: International Commission on Radiation Units and Measurements. 1996.

[24] Richard S, Husarik DB, Yadava G, Murphy SN, Samei E. Towards task-based assessment of CT performance: system and object MTF across different reconstruction algorithms. Med Phys. 2012;39:4115-22.

[25] Burgess AE, Li X, Abbey CK. Visual signal detectability with two noise components: anomalous masking effects. J Opt Soc Am A Opt Image Sci Vis. 1997;14:2420-42.

[26] Christianson O, Chen JJ, Yang Z, Saiprasad G, Dima A, Filliben JJ, et al. An Improved Index of Image Quality for Task-based Performance of CT Iterative Reconstruction across Three Commercial Implementations. Radiology. 2015;275:725-34.

[27] Barten P. Contrast sensitivity of the human eye and its effects on image quality. Eindhoven: Technische Universiteit Eindhoven.

[28] Webster MA, Miyahara E. Contrast adaptation and the spatial structure of natural images. J Opt Soc Am A Opt Image Sci Vis. 1997;14:2355-66.

[29] Eckstein MP, Abbey CK, Bochud FO. Visual signal detection in structured backgrounds. IV. Figures of merit for model performance in multiple-alternative forced-choice detection tasks with correlated responses. J Opt Soc Am A Opt Image Sci Vis. 2000;17:206-17.

[30] Greffier J, Boccalini S, Beregi JP, Vlassenbroek A, Vuillod A, Dupuis-Girod S, et al. CT dose optimization for the detection of pulmonary arteriovenous malformation (PAVM): A phantom study. Diagn Interv Imaging. 2020.

[31] Greffier J, Frandon J, Pereira F, Hamard A, Beregi JP, Larbi A, et al. Optimization of radiation dose for CT detection of lytic and sclerotic bone lesions: a phantom study. Eur Radiol. 2020;30:1075-8.

[32] Ott JG, Becce F, Monnin P, Schmidt S, Bochud FO, Verdun FR. Update on the non-prewhitening model observer in computed tomography for the assessment of the adaptive statistical and model-based iterative reconstruction algorithms. Phys Med Biol. 2014;59:4047-64.

[33] Rotzinger DC, Racine D, Beigelman-Aubry C, Alfudhili KM, Keller N, Monnin P, et al. Task-Based Model Observer Assessment of A Partial Model-Based Iterative Reconstruction Algorithm in Thoracic Oncologic Multidetector CT. Sci Rep. 2018;8:17734.

[34] Samei E, Bakalyar D, Boedeker KL, Brady S, Fan J, Leng S, et al. Performance evaluation of computed tomography systems: Summary of AAPM Task Group 233. Med Phys. 2019;46:e735-e56.

[35] De Marco P, Origgi D. New adaptive statistical iterative reconstruction ASiR-V: Assessment of noise performance in comparison to ASiR. J Appl Clin Med Phys. 2018;19:275-86.

[36] Lim K, Kwon H, Cho J, Oh J, Yoon S, Kang M, et al. Initial phantom study comparing image quality in computed tomography using adaptive statistical iterative reconstruction and new adaptive statistical iterative reconstruction v. J Comput Assist Tomogr. 2015;39:443-8.

Figure legends

Figure 1. a Phantom used in the study. **b** Regions of interest (ROIs) used for the noise power spectrum (NPS) assessment. **c** ROIs used to compute the task-based transfer function (TTF) with the acrylic insert.

Figure 2. Values of noise magnitude corresponding to the square root of the Area Under the Curve of the noise power spectrum (NPS) obtained on low-energy monochromatic images as function of GSI presets and percentage of ASIR and average NPS spatial frequency according to energy levels for each dual-energy CT platform.

Figure 3. Values of average noise power spectrum spatial frequency (f_{av}) obtained on low-energy monochromatic images as function of GSI presets and percentage of ASIR

Figure 4. Values of task-based transfer function at 50% (f_{50}) obtained on low-energy monochromatic images as function of GSI presets and percentage of ASIR

Figure 5. Detectability index (d') obtained on low-energy monochromatic images as function of GSI presets and percentage of ASIR for the liver metastasis (**a**) and the hepatocellular carcinoma (HCC) (**b**).

Table 1. Acquisition parameters used for each GSI preset

Preset GSI	GSI 40	GSI 22	GSI 1
kVp	80/140	80/140	80/140
mA	360	375	630
Rotation time (s)	0.6	0.7	0.5
Pitch factor	1.375	1.375	1.375
Beam collimation (mm)	64 x 0.625	64 x 0.625	64 x 0.625
CTDIvol (mGy)	8.79	10.76	12.72

Table 2. Contrast between the hypodense liver metastasis or the hypodense hepatocellular carcinoma and surrounding the liver parenchyma as function of keV used to compute the detectability index. These values were extrapolated to the curves of HU variations measured on patients and published by Wang *et al*. [6].

Energy (keV)	Liver metastasis	Hepatocellular carcinoma
40	-112	-39
50	-78	-30
60	-61	-23
70	-50	-17
80	-43	-16

Footnote: The lesions being hypodense, their HU values were lower than the surrounding liver parenchyma and hence the resulting contrast is negative.

Table 3. Percentage variation of the detectability index (*d'*) obtained with three lowest energy levels compared to those obtained with a conventional single energy CT acquisition at 120 kVp for all dose levels, reconstruction types and for both detection tasks.

Lesions	GSI	Energy (keV)	FBP	ASIR30	ASIR50	ASIR 70	ASIR100
Liver metastasis	40	40	-39%	-37%	-31%	-26%	-20%
		50	-22%	-14%	-5%	**5%**	**18%**
		60	-3%	-2%	**2%**	**4%**	**6%**
	22	40	-39%	-35%	-29%	-22%	-6%
		50	-21%	-13%	-4%	**6%**	**33%**
		60	-3%	-3%	0%	**1%**	**14%**
	1	40	-40%	-28%	-21%	-15%	-2%
		50	-22%	-4%	**5%**	**15%**	**35%**
		60	-5%	**5%**	**7%**	**9%**	**13%**
Hepatocellular carcinoma	40	40	-40%	-36%	-29%	-23%	-11%
		50	-14%	-4%	**9%**	**22%**	**48%**
		60	**3%**	**5%**	**9%**	**12%**	**20%**
	22	40	-39%	-33%	-26%	-16%	**3%**
		50	-13%	-1%	**11%**	**28%**	**65%**
		60	**3%**	**5%**	**9%**	**14%**	**26%**
	1	40	-40%	-28%	-18%	-8%	**13%**
		50	-13%	**6%**	**21%**	**39%**	**77%**
		60	**1%**	**10%**	**15%**	**20%**	**30%**

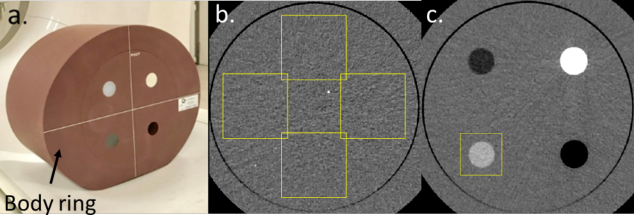
a.
b.
c.
Body ring

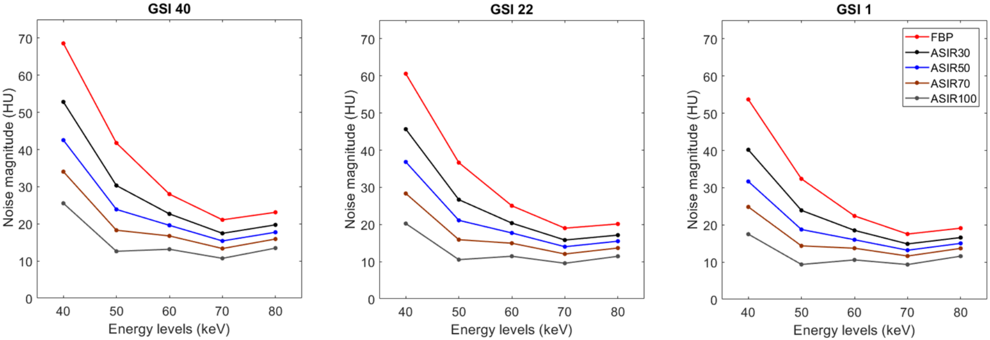
GSI 40
GSI 22
GSI 1
Noise magnitude (HU)
0
10
20
30
40
50
60
70
40
50
60
70
80
Energy levels (keV)
FBP
ASIR30
ASIR50
ASIR70
ASIR100

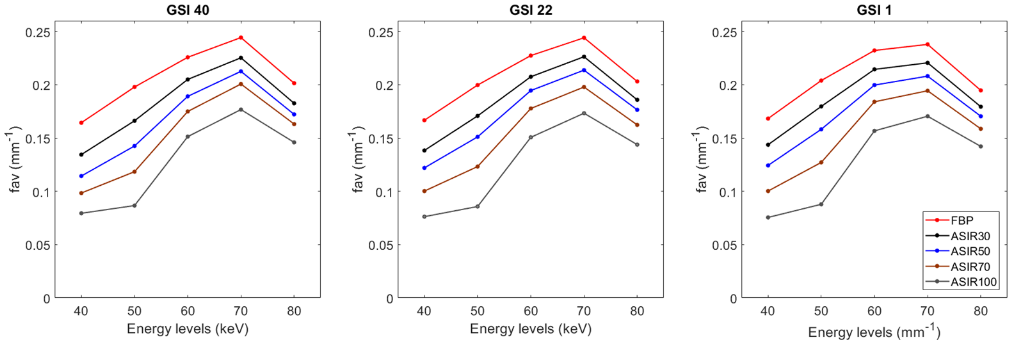
GSI 40
GSI 22
GSI 1
fav (mm^{-1})
0.25
0.2
0.15
0.1
0.05
0
40
50
60
70
80
Energy levels (keV)
Energy levels (mm^{-1})
FBP
ASIR30
ASIR50
ASIR70
ASIR100

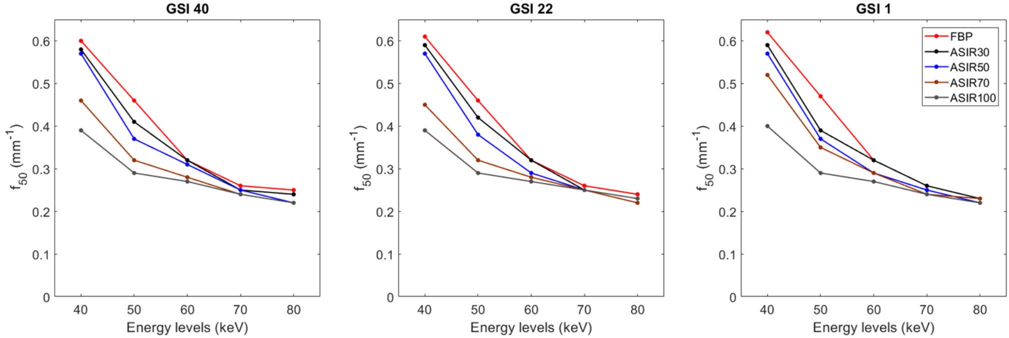
GSI 40
GSI 22
GSI 1
f_{50} (mm^{-1})
0
0.1
0.2
0.3
0.4
0.5
0.6
40
50
60
70
80
Energy levels (keV)
FBP
ASIR30
ASIR50
ASIR70
ASIR100

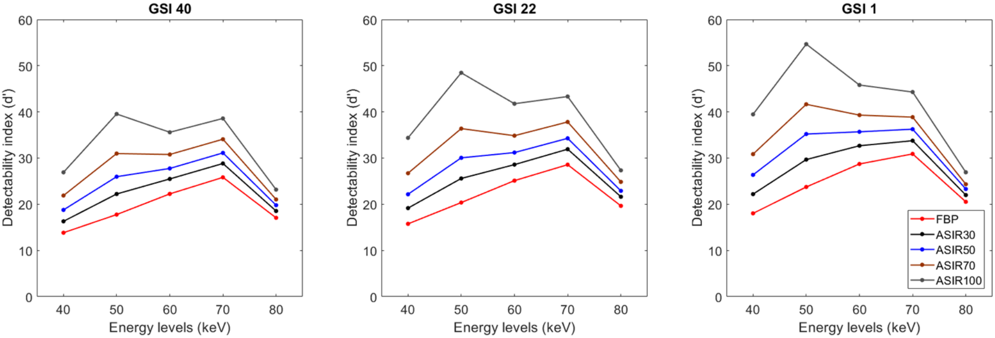

GSI 40
GSI 22
GSI 1
Detectability index (d')
Energy levels (keV)
0
10
20
30
40
50
60
40
50
60
70
80
FBP
ASIR30
ASIR50
ASIR70
ASIR100

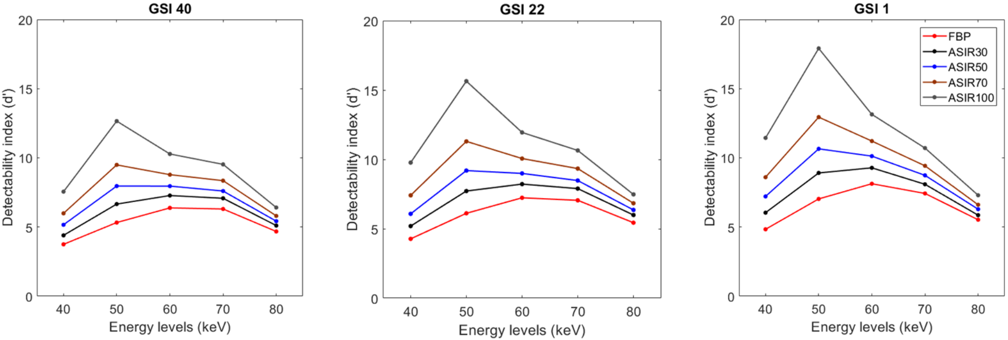
GSI 40
GSI 22
GSI 1
Detectability index (d')
Energy levels (keV)
0
5
10
15
20
40
50
60
70
80
FBP
ASIR30
ASIR50
ASIR70
ASIR100